Strong anharmonicity and high thermoelectric efficiency in high-temperature SnS from first principles

Unai Aseginolaza,[1,2,3] Raffaello Bianco,[1] Lorenzo Monacelli,[4] Lorenzo Paulatto,[5] Matteo Calandra,[6] Francesco Mauri,[4] Aitor Bergara,[1,2,7] and Ion Errea[1,2,3]

[1]*Centro de Física de Materiales CFM, CSIC-UPV/EHU, Paseo Manuel de Lardizabal 5, 20018 Donostia, Basque Country, Spain*
[2]*Donostia International Physics Center (DIPC), Manuel Lardizabal pasealekua 4, 20018 Donostia, Basque Country, Spain*
[3]*Fisika Aplikatua 1 Saila, Gipuzkoako Ingenieritza Eskola, University of the Basque Country (UPV/EHU), Europa Plaza 1, 20018 Donostia, Basque Country, Spain*
[4]*Dipartimento di Fisica, Università di Roma Sapienza, Piazzale Aldo Moro 5, I-00185 Roma, Italy*
[5]*IMPMC, UMR CNRS 7590, Sorbonne Universités-UPMC Univ. Paris 06, MNHN, IRD, 4 Place Jussieu, F-75005 Paris, France*
[6]*Sorbonne Universités, CNRS, Institut des Nanosciences de Paris, UMR7588, F-75252 Paris, France*
[7]*Departamento de Física de la Materia Condensada, University of the Basque Country (UPV/EHU), 48080 Bilbao, Basque Country, Spain*

(Received 6 June 2019; revised manuscript received 25 October 2019; published 16 December 2019)

SnS and SnSe are isoelectronic materials with a common phase diagram. Recently, SnSe was found to be the most efficient intrinsic thermoelectric material in its high-temperature *Cmcm* phase above 800 K. Making use of first-principles calculations, here we show that the electronic and vibrational properties of both materials are very similar in this phase and, consequently, SnS is also expected to have a high thermoelectric figure of merit at high temperature in its *Cmcm* phase. In fact, the electronic power factor and lattice thermal conductivity are comparable for both materials, which ensures a similar figure of merit. As in the case of SnSe, the vibrational properties of SnS in the *Cmcm* phase are far from trivial and are dominated by huge anharmonic effects. Its phonon spectra are strongly renormalized by anharmonicity and the spectral functions of some particular in-plane modes depict anomalous non-Lorentzian profiles. Finally, we show that nonperturbative anharmonic effects in the third-order force-constants are crucial in the calculation of the lattice thermal conductivity. Our results motivate new experiments in the high-temperature regime to measure the figure of merit of SnS.

DOI: 10.1103/PhysRevB.100.214307

I. INTRODUCTION

Thermoelectricity is a technologically interesting material property that allows us to transform residual heat into useful electricity [1,2]. The efficiency of this energy transformation is controlled by the dimensionless figure of merit,

$$ZT = S^2\sigma T/\kappa, \tag{1}$$

where S is the Seebeck coefficient, σ the electrical conductivity, T the temperature, and $\kappa = \kappa_e + \kappa_l$ the sum of electronic κ_e and lattice κ_l thermal conductivities. Therefore, a good thermoelectric performance requires a high power factor $P_F = S^2\sigma$ together with a low thermal conductivity.

Monochalcogenides have proven to be efficient thermoelectric materials [3–6], mainly due to their strongly anharmonic lattice that implies a low lattice thermal conductivity [7–11]. PbTe is an appropriate example of the potential technological relevance of thermoelectric monochalcogenides: It shows a high ZT in the 600–800 K temperature range [12], as high as 2.2 when nanostructured [13], and has been successfully applied in spacecrafts [14]. In recent years, SnSe has attracted a great deal of attention since it was measured to be the most efficient intrinsic thermoelectric material [15]. Its figure of merit soars to 2.6 after a structural phase transition [15–18] at around 800 K from the low-symmetry *Pnma* phase to the high-symmetry *Cmcm*. In the high-symmetry phase the electronic band gap is reduced without affecting its ultralow thermal conductivity, providing the record ZT. A recent theoretical work shows that the phase transition [19] is second-order and nonperturbative anharmonicity is very important to get a thermal conductivity in agreement with experiments.

SnS is isoelectronic to SnSe and shows very similar electronic and vibrational properties [17,18,20] at low temperatures. Experimentally it also shows a phase transition [17,18] from the *Pnma* to the *Cmcm* structure and a very low thermal conductivity in the former [21,22] phase. Therefore, it is expected to be a very efficient thermoelectric material in the high-temperature phase, which together with the fact that S is a much more earth abundant element than Se, makes it a very interesting candidate for technological applications. Actually, in Refs. [21,22] it is shown how the ZT of undoped SnS increases very fast before the phase transition as in the case of SnSe. However, as far as we are aware, there are no experimental transport measurements for the high-temperature phase of SnS. First-principles calculations of its thermoelectric properties are also absent in the literature, hindered by the unstable modes obtained within the harmonic approximation as in the case of SnSe [23,24].

In this work, by performing *ab initio* calculations we propose that *Cmcm* SnS is expected to be a very efficient intrinsic thermoelectric material, as good as SnSe in this phase. We

show that the P_F of SnSe and SnS are expected to be very similar in this phase, as long as the electronic relaxation time is similar in both materials. By including anharmonicity in the phonon calculation at a nonperturbative level within the stochastic self-consistent harmonic approximation [25–27] (SSCHA), we show that the phonon spectrum of SnS suffers a strong anharmonic renormalization. The phase transition is driven by the collapse of a zone-border phonon. Anharmonicity is so large that the spectral function of some vibrational modes deviates from the Lorentzian-like shape as it happens in other monochalcogenides [8,11]. Finally, we calculate the lattice thermal conductivity of *Cmcm* SnS obtaining ultralow values below $\approx$1.0 $\mathrm{Wm^{-1}K^{-1}}$. Nonperturbative anharmonic corrections to the third-order force-constants are important in its calculation as it happens in SnSe [19]. There is a clear anisotropy between in-plane and out-of-plane thermal conductivities. The similarity of the power factors and the lattice thermal conductivities of SnSe and SnS suggest that the latter may be an earth abundant efficient thermoelectric material and motivate more experimental effort to measure its ZT in the high-temperature phase.

This article is organized as follows. In Sec. II we briefly review the theoretical background for the calculation of anharmonic phonons, thermal conductivity, and electronic transport properties. In Sec. III we specify the computational details. In Sec. IV we discuss the results of our work. Conclusions are given in Sec. V.

II. THEORETICAL BACKGROUND

A. Electronic transport properties

Within the semiclassical Boltzmann transport theory [28] the electrical conductivity and the Seebeck coefficient can be calculated, respectively, as

$$\sigma(T,\mu) = e^2 \int_{-\infty}^{\infty} d\varepsilon \left[-\frac{\partial f(T,\mu,\varepsilon)}{\partial \epsilon} \right] \Sigma(\varepsilon), \tag{2}$$

$$S(T,\mu) = \frac{e}{T\sigma(T,\mu)} \int_{-\infty}^{\infty} d\varepsilon \left[-\frac{\partial f(T,\mu,\varepsilon)}{\partial \epsilon} \right] \Sigma(\varepsilon)(\varepsilon - \mu), \tag{3}$$

where e is the electron charge, μ the chemical potential, $f(T,\mu,\varepsilon)$ the Fermi-Dirac distribution function, and $\Sigma(\varepsilon)$ the transport distribution function. The latter is defined as

$$\Sigma(\varepsilon) = \frac{1}{\Omega N_{\mathbf{k}}} \sum_{n\mathbf{k}} \tau^e_{n\mathbf{k}} |\mathbf{v}_{n\mathbf{k}}|^2 \delta(\varepsilon - \varepsilon_{n\mathbf{k}}), \tag{4}$$

where Ω is the unit cell volume, $N_{\mathbf{k}}$ the number of $\mathbf{k}$ points in the sum, and $\varepsilon_{n\mathbf{k}}$, $\mathbf{v}_{n\mathbf{k}}$, and $\tau^e_{n\mathbf{k}}$ are, respectively, the energy, Fermi velocity, and relaxation time of the electronic state with band index n and crystal momentum $\mathbf{k}$. Our goal here is to compare the power factors $P_F(T,\mu) = \sigma(T,\mu)S^2(T,\mu)$ of SnSe and SnS coming from their different band structure without explicitly calculating the electronic relaxation times. We thus assume that $\tau^e_{n\mathbf{k}} = \tau^e$ is just the same constant for both compounds. In these conditions it is easy to see from Eqs. (2)–(4) that the power factor is proportional to τ^e. In the following, we will limit ourselves to the analysis of $P_F(T,\mu)/\tau^e$, which only depends on the band structure of the compounds.

B. Free energy of strongly anharmonic crystals

We study the vibrational properties of SnS within the Born-Oppenheimer (BO) approximation, in which the Hamiltonian H that determines the dynamics of the ions consists of the ionic kinetic energy and the BO potential $V(\mathbf{R})$. $\mathbf{R}$ denotes $R^{\alpha s}(\mathbf{l})$ in component free notation, which specifies the atomic configuration of the crystal. α is a Cartesian direction, s labels an atom within the unit cell, and $\mathbf{l}$ a lattice vector. From now on, we will use a single composite index $a = (\alpha, s, \mathbf{l})$ and bold letters to indicate quantities in component-free notation. We will keep this composite index for Fourier transformed components adding a bar, $\bar{a}$, to distinguish that in this case $\bar{a}$ just denotes a Cartesian index and an atom in the unit cell.

As it will be shown below and as it happens in *Cmcm* SnSe [19,23,24], the harmonic approximation collapses for *Cmcm* SnS. Truncating the Taylor expansion of $V(\mathbf{R})$ for this phase at second order and diagonalizing the resulting harmonic force-constants $\boldsymbol{\phi}$ large imaginary frequencies are obtained. This makes the calculation of any thermodynamic and transport property involving phonons impossible at the harmonic level. We overcome this problem by solving the ionic Hamiltonian within the SSCHA, a variational method that includes anharmonic effects at a nonperturbative level in the calculation of the vibrational free energy [25–27].

The SSCHA performs a variational minimization of the free energy with respect to a trial density matrix $\rho_{\mathcal{H}}$ that solves an auxiliary harmonic Hamiltonian,

$$\mathcal{H} = \sum_a \frac{P_a^2}{2M_a} + \frac{1}{2} \sum_{ab} (\mathbf{R} - \boldsymbol{\mathcal{R}})_a \Phi_{ab} (\mathbf{R} - \boldsymbol{\mathcal{R}})_b, \tag{5}$$

where P is the kinetic energy and M_a the atomic mass of atom a. The variational parameters in the minimization are the $\boldsymbol{\Phi}$ force-constants, which should not be confused with the harmonic force-constants $\boldsymbol{\phi}$, and the $\boldsymbol{\mathcal{R}}$ positions. The $\boldsymbol{\mathcal{R}}$ positions are referred as the *centroid* positions, i.e., the most probable atomic positions. The $\boldsymbol{\Phi}$ force-constants are related to the broadening of the ionic wave functions around the centroid positions. At the minimum, the SSCHA yields a free energy F that takes into account anharmonicity without approximating the BO potential. The minimization can be performed by calculating atomic forces and energies in stochastic atomic configurations in supercells using importance sampling and reweighting techniques [25–27]. The supercell atomic configurations are created according to the probability distribution function related to $\rho_{\mathcal{H}}$. Since the BO energy landscape is sampled stochastically, the SSCHA method does not use any fit or approximation on the $V(\boldsymbol{R})$. It is, therefore, unbiased by the starting point.

C. Free energy Hessian and second-order phase transition

In a displacive second-order phase transition, at high temperature the free energy F has a minimum in a high-symmetry

configuration ($\boldsymbol{\mathcal{R}}_{\rm hs}$), but, on lowering the temperature, $\boldsymbol{\mathcal{R}}_{\rm hs}$ becomes a saddle point at the transition temperature T_c. Therefore, the free-energy Hessian evaluated at $\boldsymbol{\mathcal{R}}_{\rm hs}$, $\partial^2 F/\partial\boldsymbol{\mathcal{R}}\partial\boldsymbol{\mathcal{R}}|_{\boldsymbol{\mathcal{R}}_{\rm hs}}$, at high temperature is positive definite but it develops one or multiple negative eigendirections at T_c. The SSCHA free-energy Hessian can be computed by using the analytic formula [26]

$$\frac{\partial^2 F}{\partial\boldsymbol{\mathcal{R}}\partial\boldsymbol{\mathcal{R}}} = \overset{(3)}{\boldsymbol{\Phi}} + \overset{(3)}{\boldsymbol{\Phi}}\boldsymbol{\Lambda}(0)\big[\mathbf{1} - \overset{(4)}{\boldsymbol{\Phi}}\boldsymbol{\Lambda}(0)\big]^{-1}\overset{(3)}{\boldsymbol{\Phi}}, \tag{6}$$

with

$$\overset{(n)}{\boldsymbol{\Phi}} = \left\langle \frac{\partial^n V}{\partial \mathbf{R}^n} \right\rangle_{\rho_{\mathcal{H}}}. \tag{7}$$

Here $\langle\rangle_{\rho_{\mathcal{H}}}$ denotes the quantum statistical average taken with the density matrix $\rho_{\mathcal{H}}$. All these averages are evaluated here stochastically as described in Ref. [26]. The $\overset{(n)}{\boldsymbol{\Phi}}$ nonperturbative nth-order force-constants should not be confused with the nth-order perturbative force-constants $\overset{(n)}{\boldsymbol{\phi}}$, which are calculated as derivatives of the BO potential at a reference position 0 and not as quantum statistical averages:

$$\overset{(n)}{\boldsymbol{\phi}} = \left[\frac{\partial^n V}{\partial \mathbf{R}^n}\right]_0. \tag{8}$$

In Eq. (6) the value $z = 0$ of the fourth-order tensor $\boldsymbol{\Lambda}(z)$ is used. For a generic complex number z it is defined, in components, by

$$\Lambda^{abcd}(z) = -\frac{1}{2}\sum_{\mu\nu}\tilde{F}(z,\tilde{\Omega}_\mu,\tilde{\Omega}_\nu)\sqrt{\frac{\hbar}{2M_a\tilde{\Omega}_\mu}}e^a_\mu \times\sqrt{\frac{\hbar}{2M_b\tilde{\Omega}_\nu}}e^b_\nu\sqrt{\frac{\hbar}{2M_c\tilde{\Omega}_\mu}}e^c_\mu\sqrt{\frac{\hbar}{2M_d\tilde{\Omega}_\nu}}e^d_\nu, \tag{9}$$

with $\tilde{\Omega}^2_\mu$ and e^a_μ the eigenvalues and corresponding eigenvectors of

$$D^{(S)}_{ab} = \Phi_{ab}/\sqrt{M_aM_b}, \tag{10}$$

respectively. In Eq. (9)

$$\tilde{F}(z,\tilde{\Omega}_\mu,\tilde{\Omega}_\nu) = \frac{2}{\hbar}\left\{\frac{(\tilde{\Omega}_\mu+\tilde{\Omega}_\nu)[1+n_B(\tilde{\Omega}_\mu)+n_B(\tilde{\Omega}_\nu)]}{(\tilde{\Omega}_\mu+\tilde{\Omega}_\nu)^2-z^2} - \frac{(\tilde{\Omega}_\mu-\tilde{\Omega}_\nu)[n_B(\tilde{\Omega}_\mu)-n_B(\tilde{\Omega}_\nu)]}{(\tilde{\Omega}_\mu-\tilde{\Omega}_\nu)^2-z^2}\right\}, \tag{11}$$

where $n_B(\omega) = 1/(e^{\beta\hbar\omega}-1)$ is the bosonic occupation number. Evaluating through Eq. (6) the free-energy Hessian at $\boldsymbol{\mathcal{R}}_{\rm hs}$ and studying its spectrum as a function of temperature, we can predict the occurrence of a displacive phase transition and estimate T_c. This technique has been successful to study phase-transition temperatures in high-pressure hydrides, monochalcogenides, and transition metal dichalcogenides undergoing charge-density wave transitions [11,29,30].

D. Dynamical properties of solids and phonon frequencies

As shown in Ref. [26], even if the SSCHA is a ground-state theory, it is possible to formulate a valid ansatz to calculate dynamical properties of crystals such as phonon spectral functions. The one-phonon Green function $\mathbf{G}(z)$ for the variable $\sqrt{M_a}(R_a - \mathcal{R}_a)$ can be calculated as

$$\mathbf{G}^{-1}(z) = z^2\mathbf{1} - \mathbf{M}^{-\frac{1}{2}}\boldsymbol{\Phi}\mathbf{M}^{-\frac{1}{2}} - \boldsymbol{\Pi}(z). \tag{12}$$

With this definition, in the static limit the Green function becomes the dynamical matrix obtained with the free-energy Hessian: $\mathbf{G}^{-1}(0) = -\mathbf{D}^{(F)}$, with

$$D^{(F)}_{ab} = \frac{1}{\sqrt{M_aM_b}}\frac{\partial^2 F}{\partial\mathcal{R}_a\partial\mathcal{R}_b}. \tag{13}$$

We will label with ω_μ the eigenvalues of $\mathbf{D}^{(F)}$. The SSCHA self-energy is given by

$$\boldsymbol{\Pi}(z) = \mathbf{M}^{-\frac{1}{2}}\overset{(3)}{\boldsymbol{\Phi}}\boldsymbol{\Lambda}(z)\big[\mathbf{1} - \overset{(4)}{\boldsymbol{\Phi}}\boldsymbol{\Lambda}(z)\big]^{-1}\overset{(3)}{\boldsymbol{\Phi}}\mathbf{M}^{-\frac{1}{2}}, \tag{14}$$

where $M_{ab} = \delta_{ab}M_a$ is the mass matrix. We have explicitly verified that neglecting $\overset{(4)}{\boldsymbol{\Phi}}$ in Eq. (6) has a completely negligible impact on the eigenvalues of $\mathbf{D}^{(F)}$. We consistently neglect $\overset{(4)}{\boldsymbol{\Phi}}$ in Eq. (12) as well. This reduces the SSCHA self energy to the so-called bubble self energy, namely,

$$\boldsymbol{\Pi}(z) \approx \boldsymbol{\Pi}^{(B)}(z) = \mathbf{M}^{-\frac{1}{2}}\overset{(3)}{\boldsymbol{\Phi}}\boldsymbol{\Lambda}(z)\overset{(3)}{\boldsymbol{\Phi}}\mathbf{M}^{-\frac{1}{2}}. \tag{15}$$

The cross section in an inelastic, e.g., neutron, experiment is proportional to the spectral function $\sigma(\omega) = -\omega\mathrm{Tr}\mathrm{Im}\mathbf{G}(\omega + i0^+)/\pi$ [31]. Its peaks signal the presence of collective vibrational excitations (phonons) having certain energies and linewidth. To recognize the contribution of each phonon mode to this spectral function, we first take advantage of the lattice periodicity and Fourier transform the spectral function and the self energy, and second we neglect the mixing between phonon modes and assume that $\boldsymbol{\Pi}(z)$ is diagonal in the basis of the eigenvectors:

$$\Pi_\mu(\mathbf{q},\omega) = \sum_{\bar{a}\bar{b}} e^{\bar{a}}_\mu(-\mathbf{q})\Pi_{\bar{a}\bar{b}}(\mathbf{q},\omega+i0^+)e^{\bar{b}}_\mu(\mathbf{q}). \tag{16}$$

The cross section is then given by

$$\sigma(\mathbf{q},\omega) = \frac{1}{\pi}\sum_\mu \frac{-\omega\mathrm{Im}\Pi_\mu(\mathbf{q},\omega)}{\big[\omega^2 - \tilde{\Omega}^2_\mu(\mathbf{q}) - \mathrm{Re}\Pi_\mu(\mathbf{q},\omega)\big]^2 + [\mathrm{Im}\Pi_\mu(\mathbf{q},\omega)]^2}. \tag{17}$$

In Eqs. (16) and (17) $\tilde{\Omega}^2_\mu(\mathbf{q})$ and $e^{\bar{a}}_\mu(\mathbf{q})$ are, respectively, the eigenvalues and eigenvectors of $\mathbf{D}^{(S)}(\mathbf{q})$, the Fourier transform of Eq. (10).

The cross section calculated as in Eq. (17) does not have any given lineshape. However, when $\Pi_\mu(\mathbf{q},\omega)$ is small compared to $\tilde{\Omega}^2_\mu(\mathbf{q})$, it is justified to approximate $\Pi_\mu(\mathbf{q},\omega) \sim \Pi_\mu[\mathbf{q},\tilde{\Omega}_\mu(\mathbf{q})]$, which turns $\sigma(\mathbf{q},\omega)$ into a sum of Lorentzian functions. In this Lorentzian approximation the peaks appear at the $\Omega_\mu(\mathbf{q})$ phonon frequencies, with

$$\Omega^2_\mu(\mathbf{q}) = \tilde{\Omega}^2_\mu(\mathbf{q}) + \mathrm{Re}\Pi_\mu[\mathbf{q},\tilde{\Omega}_\mu(\mathbf{q})], \tag{18}$$

and the linewidths are proportional to $\mathrm{Im}\{\Pi_\mu[\mathbf{q},\tilde{\Omega}_\mu(\mathbf{q})]\}$.

E. Thermal conductivity

We calculate the lattice thermal conductivity within the single mode relaxation time approximation (SMA) [32] making use of the eigenvalues and eigenvectors of $\mathbf{D}^{(S)}(\mathbf{q})$ (as it will be shown below it is not possible at the harmonic level due to the instabilities obtained) as well as the nonperturbative third-order force-constants $\overset{(3)}{\mathbf{\Phi}}$. In the SMA the lattice thermal conductivity is written as follows [33]:

$$\kappa_l^{\alpha\beta} = \frac{\hbar^2}{\Omega N_{\mathbf{q}} k_B T^2} \sum_{\mathbf{q}\mu} c_\mu^\alpha(\mathbf{q}) c_\mu^\beta(\mathbf{q}) \tilde{\Omega}_\mu^2(\mathbf{q}) n_B[\tilde{\Omega}_\mu(\mathbf{q})] \times \{n_B[\tilde{\Omega}_\mu(\mathbf{q})] + 1\} \tau_\mu(\mathbf{q}), \tag{19}$$

where, for the phonon mode μ with momentum $\mathbf{q}$, $c_\mu^\alpha(\mathbf{q})$ is the Cartesian component α of its lattice group velocity and $\tau_\mu(\mathbf{q})$ its lifetime. $N_{\mathbf{q}}$ is the number of $\mathbf{q}$ points used in the sum. The Bose-Einstein occupation of each mode is given by the Boltzmann transport equation (BTE) and the inverse phonon lifetime [with $\gamma_\mu(\mathbf{q})$ the half width at half maximum] is calculated as [33]

$$\frac{1}{\tau_\mu(\mathbf{q})} = 2\gamma_\mu(\mathbf{q}) = \frac{\pi}{\hbar^2 N_{\mathbf{q}}} \sum_{\mathbf{q}'\nu\eta} \left|\overset{(3)}{\Phi}_{\mu\nu\eta}(\mathbf{q}, \mathbf{q}', \mathbf{q}'')\right|^2 \times (\{1 + n_B[\tilde{\Omega}_\nu(\mathbf{q}')] + n_B[\tilde{\Omega}_\eta(\mathbf{q}'')]\} \delta[\tilde{\Omega}_\mu(\mathbf{q}) - \tilde{\Omega}_\nu(\mathbf{q}') - \tilde{\Omega}_\eta(\mathbf{q}'')] + 2\{n_B[\tilde{\Omega}_\nu(\mathbf{q}')] - n_B[\tilde{\Omega}_\eta(\mathbf{q}'')]\} \delta[\tilde{\Omega}_\mu(\mathbf{q}) + \tilde{\Omega}_\nu(\mathbf{q}') - \tilde{\Omega}_\eta(\mathbf{q}'')]), \tag{20}$$

with $\mathbf{q} + \mathbf{q}' + \mathbf{q}'' = \mathbf{G}$, $\mathbf{G}$ being a reciprocal lattice vector. Here $\overset{(3)}{\Phi}_{\mu\nu\eta}(\mathbf{q}, \mathbf{q}', \mathbf{q}'')$ is the third-order force-constants matrix written in the space of the normal modes:

$$\overset{(3)}{\Phi}_{\mu\nu\eta}(\mathbf{q}, \mathbf{q}', \mathbf{q}'') = \sum_{\bar{a}\bar{b}\bar{c}} \sqrt{\frac{\hbar^3}{8 M_{\bar{a}} M_{\bar{b}} M_{\bar{c}} \tilde{\Omega}_\mu(\mathbf{q}) \tilde{\Omega}_\nu(\mathbf{q}') \tilde{\Omega}_\eta(\mathbf{q}'')}} \times e_\mu^{\bar{a}}(\mathbf{q}) e_\nu^{\bar{b}}(\mathbf{q}') e_\eta^{\bar{c}}(\mathbf{q}'') \overset{(3)}{\Phi}_{\bar{a}\bar{b}\bar{c}}(\mathbf{q}, \mathbf{q}', \mathbf{q}''), \tag{21}$$

where $\overset{(3)}{\Phi}_{\bar{a}\bar{b}\bar{c}}(\mathbf{q}, \mathbf{q}', \mathbf{q}'')$ are the Fourier transformed nonperturbative third-order force-constants. We also calculate the thermal conductivity with the perturbative third-order force-constants by substituting the nonperturbative $\overset{(3)}{\mathbf{\Phi}}$ by the perturbative $\overset{(3)}{\boldsymbol{\phi}}$ in Eqs. (20) and (21).

III. COMPUTATIONAL DETAILS

We calculate the electronic bands using *ab initio* density functional theory (DFT) calculations within the local density approximation (LDA)[34] and the generalized gradient approximation in the Perdew-Burke-Ernzerhof (PBE) parametrization[35] as implemented in the QUANTUM ESPRESSO[36,37] software package. Harmonic phonons and

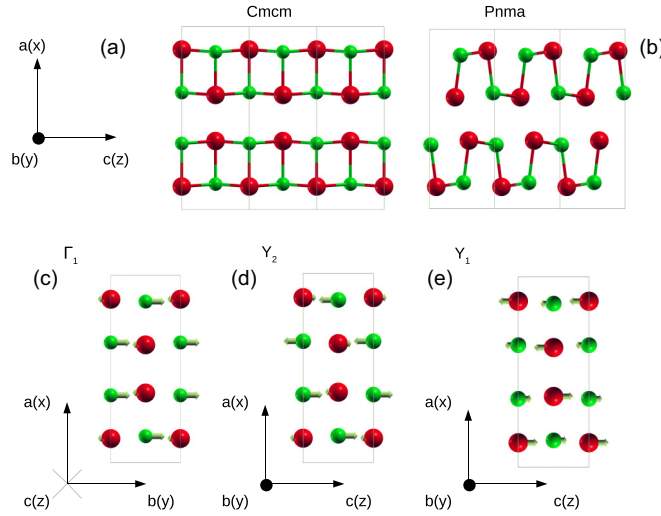

FIG. 1. XY face of the (a) *Cmcm* and (b) *Pnma* structures. Atomic displacements of modes (c) Γ_1, (d) Y_2, and (e) Y_1. Sn atoms are red and S atoms are green.

perturbative third-order force-constants $\overset{(3)}{\boldsymbol{\phi}}$ are calculated using density functional perturbation theory [33,38]. We use projector augmented wave [39] (PAW) pseudopotentials that include $5s^2\ 5p^2\ 4d^{10}$ electrons in the case of Sn and $3s^2\ 3p^4$ in the case of S or Se. For the perturbative third-order force-constants we use norm-conserving pseudopotentials, which were shown [19] to provide very similar third-order force-constants compared to the PAW result. A $16 \times 16 \times 16$ sampling of the first Brillouin zone of the primitive cell and an energy cutoff of 70 Ry are employed for the DFT self-consistent calculation. For the electronic transport calculations we use the Boltztrap software package [40]. For the sum in Eq. (4) we perform a non self-consistent DFT calculation in a $30 \times 30 \times 30$ sampling of the first Brillouin zone. We use experimental lattice parameters at the transition temperature as we got better agreement with experiments for SnSe in a previous work [19]. The experimental lattice parameters taken from Refs. [16,17] are $a = 22.13$ a$_0$, $b = 8.13$ a$_0$, $c = 8.13$ a$_0$ for SnSe and $a = 21.69$ a$_0$, $b = 7.84$ a$_0$, $c = 7.84$ a$_0$ (a$_0$ is the Bohr length) for SnS. The structures of the high-temperature *Cmcm* and low-temperature *Pnma* phases are shown in Fig. 1.

Anharmonic phonons and nonperturbative third-order force-constants are calculated within the SSCHA using a $2 \times 2 \times 2$ supercell. For the SSCHA calculation we use forces calculated within DFT. Once we get the anharmonic force-constants, we substract the harmonic ones and interpolate the difference to a $6 \times 6 \times 6$ grid. Then, we add this interpolated difference to the harmonic dynamical matrices in a $6 \times 6 \times 6$ grid, which yields anharmonic force-constants in a fine grid. By Fourier interpolating the latter we can calculate phonon frequencies at any point in the Brillouin zone. We impose the acoustic sum rule to the third-order force-constants with an iterative method prior to their Fourier interpolation [19,33]. The lattice thermal conductivity is calculated with Eq. (19) using a $10 \times 10 \times 10$ grid. For the calculation of the phonon linewidths we use a $20 \times 20 \times 20$ mesh in Eq. (20) with a Gaussian smearing of 1 cm^{-1} for the Dirac δs.

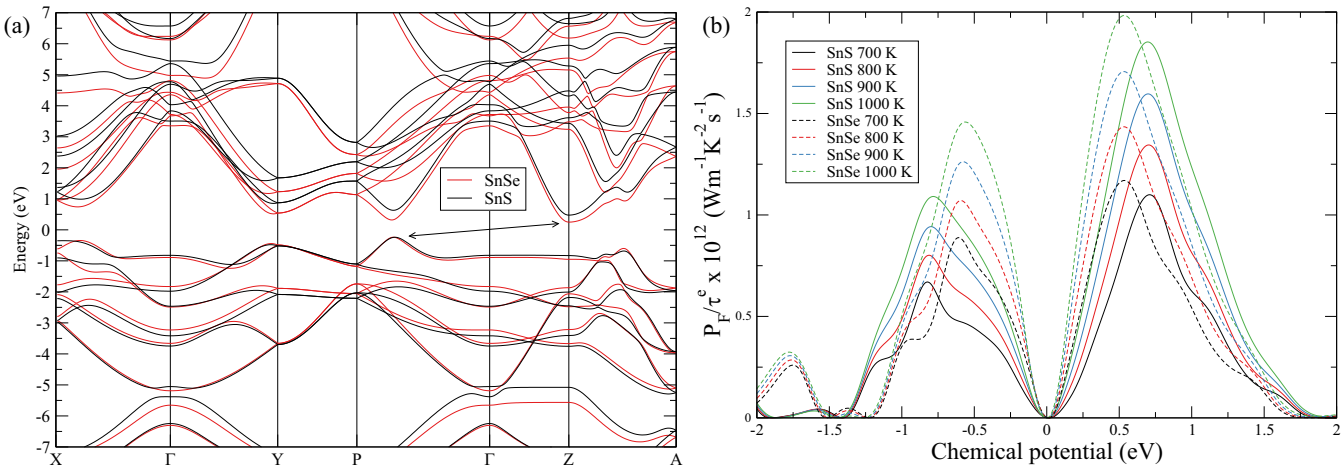

FIG. 2. (a) Electronic band structure of *Cmcm* SnS and SnSe using experimental lattice parameters. (b) PF/τ^e of *Cmcm* SnS and SnSe for different temperatures as a function of the chemical potential. The 0 value corresponds to the middle of the gap in both figures.

IV. RESULTS AND DISCUSSION

A. Electronic transport

Figure 2(a) shows the electronic band structures of SnS and SnSe in the high symmetry phase. It shows that the electronic properties of these materials are very similar because their electronic band structures are basically the same as expected for isoelectronic compounds with the same atomic structure. The major difference is that the indirect [the conduction and valence bands that constitute the gap are denoted with an arrow in Fig. 2(a)] energy gap (0.45 eV for SnSe and 0.7 eV for SnS) is bigger in the case of SnS, in agreement with experiments [15,41] and previous calculations [20]. As expected, the calculated electronic gaps within LDA underestimate the experimental values (0.86–0.948 eV for SnSe and 0.9–1.142 eV for SnS). Using these band structures we have calculated the Seebeck coefficient, which within the approximation of a constant electronic relaxation time it is independent of it, and the electrical conductivity over the electronic relaxation time σ/τ^e. The Seebeck coefficient is very similar for both materials, but σ/τ^e is slightly larger in the case of SnSe due to the smaller electronic gap. Using these two quantities we have calculated P_F/τ^e, shown in Fig. 2(b). As we can see, P_F/τ^e is very similar for both materials, but slightly higher in the case of SnSe. This is in qualitative agreement with the calculations in the low-temperature phases of SnS and SnSe [20], where the electrical conductivities and Seebeck coefficients of both materials are similar in the low-temperature phase. This justifies, in qualitative terms, the same constant relaxation time for both materials in the high-temperature phase. As we can see, P_F/τ^e increases with temperature and the difference between the maxima of SnSe and SnS is less than 5% at 1000 K. The application of a scissor operator to match the band gaps with the experimental ones just slightly changes the doping level needed to reach the maximum power factor. These results make clear that regarding the electronic transport properties these two materials are very similar in the high-temperature phase provided that the relaxation time for the electrons is similar for both materials, which is expected for isoelectronic and isostructural compounds.

B. *Pnma* to *Cmcm* phase transition

As it was already pointed out [17,19], symmetry [42,43] dictates that it is possible to have a second-order phase transition between the *Cmcm* and *Pnma* phases. The transition is dominated by the distortion pattern associated to a nondegenerate mode (Y_1) at the zone border Y point. This means [19] that, in a second-order displacive phase transition scenario, the transition temperature T_c is defined as $\partial^2 F/\partial Q^2(T = T_c) = 0$, where Q is the order parameter that transforms the system continuously from the *Pnma* ($Q \neq 0$) to the *Cmcm* ($Q = 0$) phase. As the distortion is dominated by the Y_1 phonon, $\partial^2 F/\partial Q^2(T)$ is proportional to $\omega^2_{Y_1}(T)$, which we can calculate diagonalizing $\mathbf{D}^{(F)}$.

Figure 3 shows $\omega^2_{Y_1}(T)$ within the LDA and PBE approximations. As in the case of SnSe [19], the second derivative

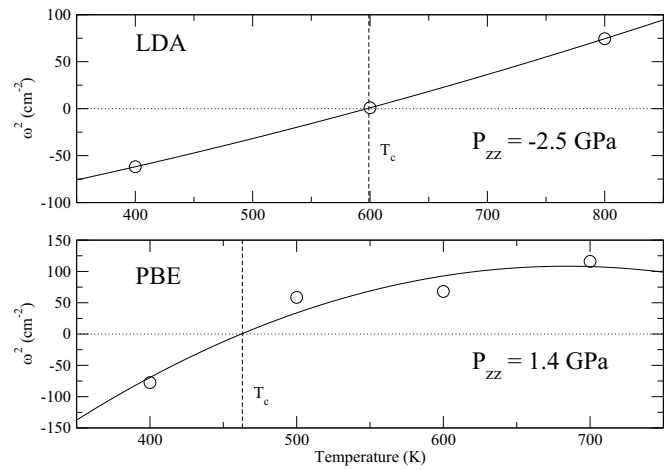

FIG. 3. $\omega^2_{Y_1}$ as a function of temperature within LDA and PBE approximations using the experimental lattice parameters (circles). The solid lines correspond to a polynomial fit. We include the pressure component P_{zz}, which is the pressure in the direction where the atoms move in the transition. This pressure is calculated including the anharmonic vibrational energy within the SSCHA as discussed in Ref. [27].

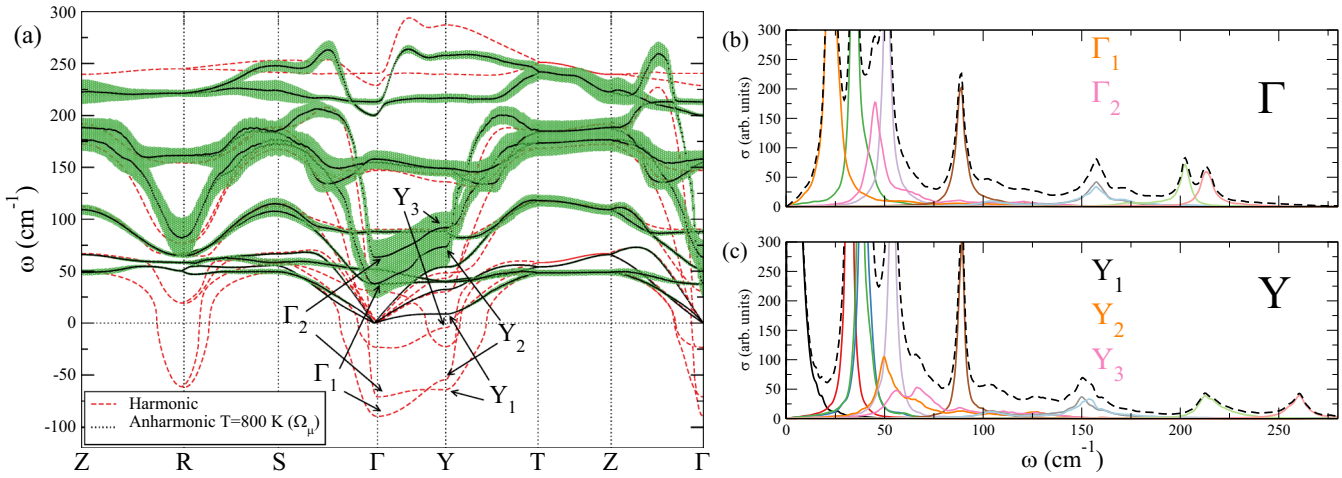

FIG. 4. (a) Harmonic and anharmonic $[\Omega_\mu(\mathbf{q})]$ phonon spectra within the Lorentzian approximation. The length of the bars corresponds to the linewidth (full length of the line is the full width at half maximum). The calculations are done within the LDA using $\overset{(3)}{\Phi}$ at 800 K and $\tilde{\Omega}_\mu(\mathbf{q})$ at 800 K. (b, c) $\sigma(\omega)$ spectral functions at the points Γ and Y, respectively, calculated as in Eq. (17). Solid lines correspond to individual modes and dashed lines are the total spectral functions.

of the free energy is positive at high temperatures and decreases lowering the temperature. For both approximations, it becomes negative at the critical temperature T_c, which means that the *Pnma* phase is not any longer a minimum of the free energy and the structure distorts adopting the *Pnma* phase. T_c strongly depends on the approximation of the exchange-correlation functional: It is 600 K for LDA and 465 K for PBE. Our LDA calculation agrees better with the experimental value, around 900 K [17]. We associate the discrepancy between LDA and PBE to the different pressures obtained in the transition direction, P_{zz}. In fact, as shown in the case of SnSe [19], T_c depends strongly on the pressure in this z direction. The pressure in Fig. 3 includes anharmonic vibrational effects on the energy following the procedure outlined in Ref. [27]. For the same lattice parameter LDA displays a much smaller pressure, as generally LDA predicts smaller lattice volumes than PBE. The underestimation with respect to experiments may be attributed to the small supercell size used for the SSCHA calculations ($2 \times 2 \times 2$). Even if experimentally T_c is around 100 K higher in SnS than in SnSe, our LDA calculations give basically the same transition temperature for both materials as $T_c = 616$ K in SnSe according to our previous calculations [19]. However, within PBE SnSe does show a lower transition temperature since $T_c = 299$ K for SnSe K [19].

C. Anharmonic phonons

Figure 4(a) compares the harmonic phonon spectrum with the anharmonic one calculated within the Lorentzian approximation at 800 K within the LDA. In the anharmonic spectrum shown the phonon energies correspond to the $\Omega_\mu(\mathbf{q})$ values of Eq. (18). The linewidth obtained in the Lorentzian approximation is also shown. The phonon spectrum suffers from a huge anharmonic renormalization. The harmonic spectrum shows broad instabilities, which are stabilized by anharmonicity. The harmonic phonons of SnS in the relaxed structure show only two instabilities, Γ_2 and Y_1. The volume increase in the experimental cell is responsible for the appearance of additional instabilities that are stabilized by anharmonic effects. The Y_1 mode is unstable below the transition temperature, but it is stabilized after the transition. By having a look at the the phonon linewidths, we can see that two modes at the Γ point (Γ_1 and Γ_2) not only suffer a strong anharmonic renormalization, but they also have a large linewidth compared to the rest of the modes in the first Brillouin zone. These modes describe optical in-plane atomic displacements (see Fig. 1, Γ_2 has the same atomic displacements as Γ_1 but in the other in-plane direction), which are the same atomic displacements of Y_2 and Y_3 at the point Y with a different periodicity due to the different momentum. The Y_2 and Y_3 in-plane modes also show a very large linewidth. On the contrary, the linewidth of mode Y_1 is not so large even if it is responsible for the phase transition (see Fig. 1).

In strongly anharmonic materials [7,8,11,19,29,44], the phonon spectral functions $\sigma(\mathbf{q}, \omega)$ show broad peaks, shoulders, and satellite peaks that cannot be captured by the simple Lorentzian picture. In Figs. 4(b) and 4(c) we show the spectral function keeping the full frequency dependence on the self-energy [see Eq. (17)]. The calculation is done for the Γ and Y points. The great majority of the modes describe a Lorentzian shape. However, the modes with a large linewidth within the Lorentzian approximation [see Fig. 4(a)] are those that clearly deviate from the Lorentzian profile (Γ_1, Γ_2, Y_2, Y_3). This non-Lorentzian shape makes clear that these modes are strongly anharmonic and the frequency dependence of the self-energy is crucial to account for their spectral function. In this case, as we can see in in Figs. 4(b) and 4(c), the non-Lorentzian shapes of the strongly anharmonic modes do not create appreciable shoulders or satellite peak in the total spectral function, however, their contribution is far from trivial.

D. Lattice thermal transport

In Fig. 5(a) we show the lattice thermal conductivity of *Cmcm* SnS as a function of temperature calculated using

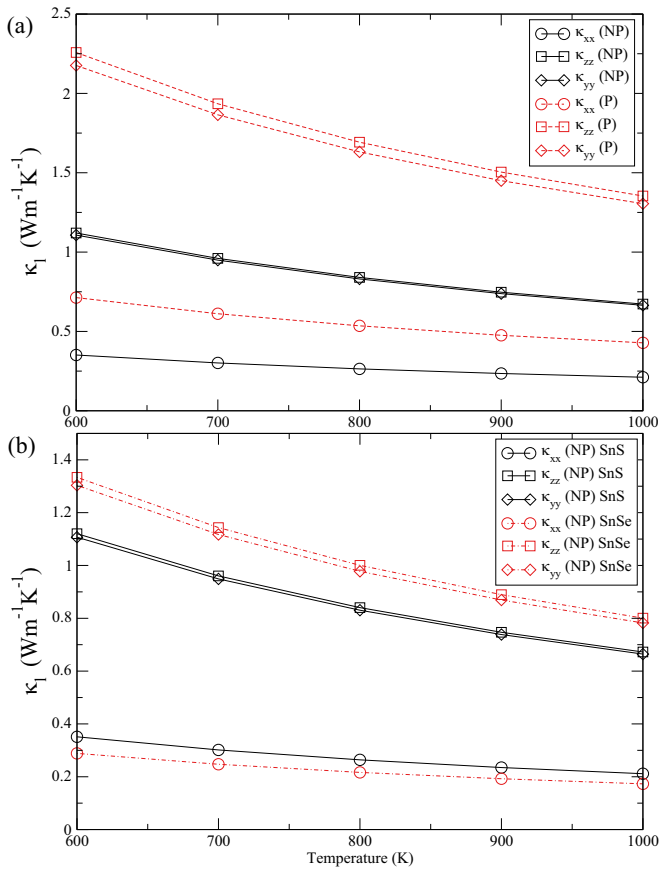

FIG. 5. (a) Lattice thermal conductivity of *Cmcm* SnS calculated within nonperturbative (NP) and perturbative (P) approaches. We have used $\tilde{\Omega}_\mu(\mathbf{q})$ at 800 K for both and $\overset{(3)}{\mathbf{\Phi}}$ at 800 K for the nonperturbative calculation in both cases. Calculations are within the LDA. (b) Lattice thermal conductivity of *Cmcm* SnS and SnSe calculated within the nonperturbative (NP) approach.

$\overset{(3)}{\mathbf{\Phi}}$ and $\overset{(3)}{\boldsymbol{\phi}}$ for solving the BTE within the SMA. We recall that $\overset{(3)}{\mathbf{\Phi}}$ are nonperturbative third-order force-constants calculated using Eq. (7) and $\overset{(3)}{\boldsymbol{\phi}}$ are perturbative third-order force-constants calculated using Eq. (8). In Fig. 5(b) we show the lattice thermal conductivities of *Cmcm* SnS and SnSe using $\overset{(3)}{\mathbf{\Phi}}$. We can see that the nonperturbative calculation using $\overset{(3)}{\mathbf{\Phi}}$ is lower than the perturbative one using $\overset{(3)}{\boldsymbol{\phi}}$ for the three Cartesian directions. This result makes clear that the nonperturbative anharmonicity is very important to calculate the thermal conductivity in this kind of thermoelectric materials. By looking at the values of the lattice thermal conductivity we can see that both materials show very similar ultralow values, below $\approx$1.0 Wm^{-1}K^{-1}. In-plane results are slightly higher for SnSe and out-of-plane calculations higher for SnS. In-plane results are against physical intuition as materials with heavier elements are supposed to have lower thermal conductivity. However, the same counterintuitive effect has been calculated for the low-temperature *Pnma* phase as well [20,45]. Experimentally the situation for the the *Pnma* phase is not so clear as, even if there is a work [46] where it is shown that the thermal conductivity of SnSe is higher than the one of SnS, more recent experiments do not agree in the value of the thermal conductivity [21,22]. In our calculations both materials show a clear anisotropy between in-plane and out-of-plane calculations in agreement with experimental results [47] for the low-temperature phase close to the phase transition. Our calculations show that SnS and SnSe have very similar thermal conductivities in the three Cartesian directions.

V. CONCLUSIONS

In conclusion, we have calculated the electronic and vibrational transport properties of *Cmcm* SnS using first-principles calculations. We have seen that the electronic transport properties of SnS and SnSe are comparable and that a similar power factor is expected for these isoelectronic and isostructural compounds. As in the case of SnSe, SnS suffers a second-order phase transition from the *Cmcm* to the *Pnma* phase driven by the collapse of a zone border phonon. We have also seen that SnS shows a strongly anharmonic phonon spectrum. Many phonon modes have a very large linewidth and show non-Lorentzian profiles in the spectral function. Finally, we have calculated the lattice thermal conductivity of *Cmcm* SnS and we have seen that nonperturbative anharmonicity substantially corrects the third-order force-constants. The thermal conductivity of both materials is very similar and ultralow. Therefore, by comparing the electronic and vibrational transport properties of SnS and SnSe in the *Cmcm* high-temperature phase, we conclude both should be good thermoelectrics. Thus, we suggest that SnS may be an earth-abundant very efficient high-temperature thermoelectric material. Experimentally, the figure of merit of SnSe is higher than the one of SnS, however, the SnSe samples are known to be porous, therefore, our work motivates more experimental effort in the figure of merit of fully dense SnSe. This work also motivates experimental effort in the high-temperature regime of SnS for its characterization.

ACKNOWLEDGMENTS

Financial support was provided by the Spanish Ministry of Economy and Competitiveness (Grant No. FIS2016-76617-P); and the Department of Education, Universities and Research of the Basque Government and the University of the Basque Country (Grant No. IT756-13). U.A. is also thankful to the Material Physics Center for a predoctoral fellowship. Computer facilities were provided by the Donostia International Physics Center (DIPC), PRACE (Grant No. 2017174186) and DARI (Grant No. A0050901202).

[1] H. J. Goldsmid, *Introduction to Thermoelectricity* (Springer, Berlin, 2010), Vol. 121.

[2] K. Behnia, *Fundamentals of Thermoelectricity* (Oxford University Press, Oxford, 2015).

[3] J. P. Heremans, V. Jovovic, E. S. Toberer, A. Saramat, K. Kurosaki, A. Charoenphakdee, S. Yamanaka, and G. J. Snyder, Science **321**, 554 (2008).

[4] Q. Zhang, B. Liao, Y. Lan, K. Lukas, W. Liu, K. Esfarjani, C. Opeil, D. Broido, G. Chen, and Z. Ren, Proc. Natl. Acad. Sci. USA **110**, 13261 (2013).

[5] S. H. Yang, T. Zhu, T. Sun, J. He, S. Zhang, and X. Zhao, Nanotechnology **19**, 245707 (2008).

[6] J. Y. Cho, X. Shi, J. R. Salvador, G. P. Meisner, J. Yang, H. Wang, A. A. Wereszczak, X. Zhou, and C. Uher, Phys. Rev. B **84**, 085207 (2011).

[7] O. Delaire, J. Ma, K. Marty, A. F. May, M. A. McGuire, M.-H. Du, D. J. Singh, A. Podlesnyak, G. Ehlers, M. Lumsden *et al.*, Nat. Mater. **10**, 614 (2011).

[8] C. W. Li, O. Hellman, J. Ma, A. F. May, H. B. Cao, X. Chen, A. D. Christianson, G. Ehlers, D. J. Singh, B. C. Sales, and O. Delaire, Phys. Rev. Lett. **112**, 175501 (2014).

[9] M. Iizumi, Y. Hamaguchi, K. F. Komatsubara, and Y. Kato, J. Phys. Soc. Jpn. **38**, 443 (1975).

[10] C. D. O'Neill, D. A. Sokolov, A. Hermann, A. Bossak, C. Stock, and A. D. Huxley, Phys. Rev. B **95**, 144101 (2017).

[11] G. A. S. Ribeiro, L. Paulatto, R. Bianco, I. Errea, F. Mauri, and M. Calandra, Phys. Rev. B **97**, 014306 (2018).

[12] I. I. Ravich, *Semiconducting Lead Chalcogenide* (Springer Science & Business Media, Berlin, 2013), Vol. 5.

[13] K. F. Hsu, S. Loo, F. Guo, W. Chen, J. S. Dyck, C. Uher, T. Hogan, E. K. Polychroniadis, and M. G. Kanatzidis, Science **303**, 818 (2004).

[14] D. M. Rowe, *Thermoelectrics Handbook: Macro to Nano* (CRC Press, Boca Raton, FL, 2018).

[15] L.-D. Zhao, S.-H. Lo, Y. Zhang, H. Sun, G. Tan, C. Uher, C. Wolverton, V. P. Dravid, and M. G. Kanatzidis, Nature (London) **508**, 373 (2014).

[16] K. Adouby, Z. Kristallogr. **213**, 343 (1998).

[17] T. Chattopadhyay, J. Pannetier, and H. Von Schnering, J. Phys. Chem. Solids **47**, 879 (1986).

[18] H. G. Von Schnering and H. Wiedemeier, Z. Kristallogr. **156**, 143 (1981).

[19] U. Aseginolaza, R. Bianco, L. Monacelli, L. Paulatto, M. Calandra, F. Mauri, A. Bergara, and I. Errea, Phys. Rev. Lett. **122**, 075901 (2019).

[20] R. Guo, X. Wang, Y. Kuang, and B. Huang, Phys. Rev. B **92**, 115202 (2015).

[21] W. He, D. Wang, J.-F. Dong, Y. Qiu, L. Fu, Y. Feng, Y. Hao, G. Wang, J. Wang, C. Liu *et al.*, J. Mater. Chem. A **6**, 10048 (2018).

[22] Q. Tan, L.-D. Zhao, J.-F. Li, C.-F. Wu, T.-R. Wei, Z.-B. Xing, and M. G. Kanatzidis, J. Mater. Chem. A **2**, 17302 (2014).

[23] J. M. Skelton, L. A. Burton, S. C. Parker, A. Walsh, C.-E. Kim, A. Soon, J. Buckeridge, A. A. Sokol, C. R. Catlow, A. Togo, and I. Tanaka, Phys. Rev. Lett. **117**, 075502 (2016).

[24] A. Dewandre, O. Hellman, S. Bhattacharya, A. H. Romero, G. K. H. Madsen, and M. J. Verstraete, Phys. Rev. Lett. **117**, 276601 (2016).

[25] I. Errea, M. Calandra, and F. Mauri, Phys. Rev. B **89**, 064302 (2014).

[26] R. Bianco, I. Errea, L. Paulatto, M. Calandra, and F. Mauri, Phys. Rev. B **96**, 014111 (2017).

[27] L. Monacelli, I. Errea, M. Calandra, and F. Mauri, Phys. Rev. B **98**, 024106 (2018).

[28] T. J. Scheidemantel, C. Ambrosch-Draxl, T. Thonhauser, J. V. Badding, and J. O. Sofo, Phys. Rev. B **68**, 125210 (2003).

[29] R. Bianco, I. Errea, M. Calandra, and F. Mauri, Phys. Rev. B **97**, 214101 (2018).

[30] R. Bianco, I. Errea, L. Monacelli, M. Calandra, and F. Mauri, Nano Lett. **19**, 3098 (2019).

[31] R. A. Cowley, Rep. Prog. Phys. **31**, 123 (1968).

[32] A. Khitun and K. L. Wang, Appl. Phys. Lett. **79**, 851 (2001).

[33] L. Paulatto, F. Mauri, and M. Lazzeri, Phys. Rev. B **87**, 214303 (2013).

[34] J. P. Perdew and A. Zunger, Phys. Rev. B **23**, 5048 (1981).

[35] J. P. Perdew, K. Burke, and M. Ernzerhof, Phys. Rev. Lett. **77**, 3865 (1996).

[36] P. Giannozzi, S. Baroni, N. Bonini, M. Calandra, R. Car, C. Cavazzoni, D. Ceresoli, G. L. Chiarotti, M. Cococcioni, I. Dabo *et al.*, J. Phys.: Condens. Matter **21**, 395502 (2009).

[37] P. Giannozzi, O. Andreussi, T. Brumme, O. Bunau, M. B. Nardelli, M. Calandra, R. Car, C. Cavazzoni, D. Ceresoli, M. Cococcioni, N. Colonna, I. Carnimeo, A. D. Corso, S. de Gironcoli, P. Delugas, R. A. DiStasio, A. Ferretti, A. Floris *et al.*, J. Phys.: Condens. Matter **29**, 465901 (2017).

[38] S. Baroni, S. De Gironcoli, A. Dal Corso, and P. Giannozzi, Rev. Mod. Phys. **73**, 515 (2001).

[39] P. E. Blöchl, Phys. Rev. B **50**, 17953 (1994).

[40] G. K. Madsen and D. J. Singh, Comput. Phys. Commun. **175**, 67 (2006).

[41] J. Vidal, S. Lany, M. d'Avezac, A. Zunger, A. Zakutayev, J. Francis, and J. Tate, Appl. Phys. Lett. **100**, 032104 (2012).

[42] D. Orobengoa, C. Capillas, M. I. Aroyo, and J. M. Perez-Mato, J. Appl. Crystallogr. **42**, 820 (2009).

[43] J. M. Perez-Mato, D. Orobengoa, and M. I. Aroyo, Acta Crystallogr. Sect. A **66**, 558 (2010).

[44] L. Paulatto, I. Errea, M. Calandra, and F. Mauri, Phys. Rev. B **91**, 054304 (2015).

[45] J. M. Skelton, L. A. Burton, A. J. Jackson, F. Oba, S. C. Parker, and A. Walsh, Phys. Chem. Chem. Phys. **19**, 12452 (2017).

[46] J. Wasscher, W. Albers, and C. Haas, Solid-State Electron. **6**, 261 (1963).

[47] D. Ibrahim, J.-B. Vaney, S. Sassi, C. Candolfi, V. Ohorodniichuk, P. Levinsky, C. Semprimoschnig, A. Dauscher, and B. Lenoir, Appl. Phys. Lett. **110**, 032103 (2017).